

Persistent fine-scale fault structure and rupture development: A new twist in the Parkfield, California, story

Clément Perrin, Felix Waldhauser, Eunseo Choi, Christopher Scholz

▶ **To cite this version:**

Clément Perrin, Felix Waldhauser, Eunseo Choi, Christopher Scholz. Persistent fine-scale fault structure and rupture development: A new twist in the Parkfield, California, story. Earth and Planetary Science Letters, 2019, 521, pp.128-138. 10.1016/j.epsl.2019.06.010 . insu-02767789

HAL Id: insu-02767789

https://insu.hal.science/insu-02767789

Submitted on 25 Oct 2021

HAL is a multi-disciplinary open access archive for the deposit and dissemination of scientific research documents, whether they are published or not. The documents may come from teaching and research institutions in France or abroad, or from public or private research centers.

L'archive ouverte pluridisciplinaire **HAL**, est destinée au dépôt et à la diffusion de documents scientifiques de niveau recherche, publiés ou non, émanant des établissements d'enseignement et de recherche français ou étrangers, des laboratoires publics ou privés.



Distributed under a Creative Commons Attribution - NonCommercial 4.0 International License

Version of Record: https://www.sciencedirect.com/science/article/pii/S0012821X19303437
Manuscript_85b7e7801b395bf7c86d54ec95ae9418

Persistent fine-scale fault structure and rupture development: a new twist in the Parkfield, California, story.

Clément Perrin[1,2,*], Felix Waldhauser[1], Eunseo Choi[3] and Christopher H. Scholz[1]

[1] Lamont Doherty Earth Observatory at Columbia University, New York, USA

[2] Present address: Université de Paris, Institut de Physique du Globe de Paris, CNRS, 75005 Paris, France

[3] Center for Earthquake Research and Information, University of Memphis, 3890 Central Ave., Memphis, TN, 38152, USA

[*] **Corresponding author: perrin@ipgp.fr**

ABSTRACT

We investigate the fine-scale geometry and structure of the San Andreas Fault near Parkfield, CA, and their role in the development of the 1966 and 2004 ~M6 earthquakes. Long-term surface fault traces indicate that structural heterogeneities associated with secondary reverse and normal fault structures are present at both rupture tips, near Middle Mountain and Gold Hill. Detailed analysis of almost 50 years of high-resolution seismicity reveals a fault plane that has been twisted into a helicoid between Middle Mountain and Gold Hill. Numerical models support our conclusion that this shape is the result of long-term torqueing of a strong stuck patch surrounded by a weak creeping region. The changes in fault friction behavior and related geometric discontinuities act as barriers to rupture propagation of moderate size earthquakes at Parkfield, and as areas of concentrations where rupture initiates. Our study demonstrates also that

© 2019 published by Elsevier. This manuscript is made available under the CC BY NC user license
https://creativecommons.org/licenses/by-nc/4.0/

smooth strike-slip faults with large cumulative offset can form new fault segments at a late stage in their evolution.

1. Introduction

The Parkfield section of the San Andreas fault is one of the best-instrumented earthquake source region in the world. Over the past 50 years, one and a half seismic cycles, including two M~6 earthquakes in 1966 and 2004, have been observed there with full geodetic and seismic coverage. Yet it is still unclear how the earthquake generation process takes place in this peculiar area.It has long been recognized that the M~6 earthquakes break a stuck patch imbedded in an otherwise creeping fault – first noted by Harris and Segall (1987) and most recently modeled by Barbot et al. (2012). It has also been observed that the rupture zone lies between two geometrical discontinuities in the fault, a slight compressional bend in the north near Middle Mountain (MM) and an extensional jog in the south near Gold Hill (GH) (Lindh and Boore, 1981). Neither the connection between these features nor their role in the nucleation and termination of the M~6 earthquake ruptures have been elucidated.

The 1966 earthquake initiated at the northern end of the rupture area near Middle Mountain, propagated unilaterally to the southeast along the entire Parkfield section and stopped near Cholame (CH) (Fig. 1 and 2; Brown et al., 1967; McEvilly et al., 1967). In contrast, the 2004 earthquake initiated in the south near Gold-Hill (GH), then propagated mainly to the northwest and stopped near MM (Fig. 1 and 2; Langbein et al., 2005; Rymer et al., 2006). Both surface ruptures were similar, formed by small fractures associated with local displacements less than 0.1 m (Brown et al., 1967; Rymer et al., 2006). Source inversion models of the 2004 event reveal two main slip patches close to either end of the rupture extent, with maximum slip ranging from 0.5 to 1m (see an

example in Fig. 3), followed by post-seismic afterslip near the surface above the coseismic rupture zone (e.g., Barbot et al., 2009; Johanson et al., 2006; Langbein et al., 2006; Murray and Langbein, 2006) but also at depth in the lower crust (Bruhat et al., 2011). Similar co-seismic distribution associated with shallow postseismic behavior has been observed for the 1966 earthquake (see an example in Fig. 3; e.g. Archuleta and Day, 1980; Scholz et al., 1969; Segall and Du, 1993).

In order to better understand rupture initiation, propagation and arrest of the two latest M6 earthquakes at Parkfield, we present here a combined analysis of high-resolution near surface and earthquake data that image the fine-scale structures of the San Andreas Fault. We bring together geologic fault information available in the literature and a broad range of satellite images and topographic data to refine the long-term surface fault traces along the Parkfield section. We also compute high-resolution seismicity recorded at the Northern California Seismic Network (NCSN) between 1969 and 2015, and aftershocks recorded during the 2 months following the 1966 earthquake (Eaton et al., 1970), spanning a nearly 50 year time period including two ~M6 events. Using these new data, we relate the structures observed at the surface to persistent deformation patterns along the three-dimensional fault plane at depth. Supported by numerical simulations of the long-term fault deformation, we propose a new mechanical model for the Parkfield segment of the San Andreas fault that differs from previous studies (e.g., Simpson et al., 2006).

2. Data analysis and results

2.1 Surface fault traces

According to the quaternary surface fault map from the USGS (U.S. Geological Survey and California Geological Survey, 2006); blue lines Fig.1b and 1c), the ~30 km long Parkfield section is composed of two linear, roughly N139°E striking, sub-parallel strands (also called the main San Andreas fault and the southwest fracture zone) that join each other at both terminations of the Parkfield section through two structural complexities : i) at the southern end near GH, an extensional jog, where the fault trace bends twice with deviations up to 28° from the mean fault strike (GH-CH, Fig.1b and 2c); ii) at the northern end, near MM, a 5° restraining bend (Lindh and Boore, 1981) (MM, Fig.1b and 2c).

We analyzed multi-resolution satellite images (Google Earth, Landsat 7) and topographic data (SRTM 30 m, LiDAR available from opentopography.org) and identified additional structural features (black lines in Fig. 1b and 1c): around MM, the active fault trace is surrounded by multiple secondary faults several kilometers away from the main San Andreas Fault and clearly imprinted in the topography (Fig. 1c). Most of them have been previously recognized as secondary strike-slip and reverse faults in the field (Thayer, 2006). Altogether they contribute to forming the localized relief observed at the center of the main fault trace. The overall shape of this structural feature, which encompasses an area approximately 5 km wide and 10 km long, resembles a restraining step-over feature that separates the locked Parkfield section from the creeping section. These secondary faults strike between N110°E and N150°E, in good agreement with earthquake locations derived in this study and focal mechanisms from Hardebeck (2010) that show oblique reverse and normal faulting (Fig. 1c; see also Thurber et al., 2006). The 1966 and 2004 earthquakes initiated and stopped near these large structural discontinuities observed at the surface near GH-CH and MM.

100 *2.2. Earthquake relocation*

101 We use seismicity data to investigate the depth extent of the heterogeneities observed
102 near the surface. We first apply a 3D grid search method (*NLLoc* program; Lomax et al.,
103 2000) to determine new absolute locations of more than ~17,000 earthquakes from
104 1966-2015 in the 3D velocity model of Thurber et al. (2006). The strike of the new 3D
105 absolute locations is rotated slightly (up to ~2°) counterclockwise compared to the
106 original NCSN locations as a result of properly accounting for the velocity variations
107 across the fault zone. We then use the double-difference algorithm *HypoDD*
108 (Waldhauser, 2001; Waldhauser and Ellsworth, 2000) to compute precise relative
109 locations using both travel-time differences from P-wave pick data (available from 1966
110 to 2015) and P- and S-wave cross correlation delay time data (1984-2015) (Schaff and
111 Waldhauser, 2005). We included all events with at least 4 stations in order to be able to
112 simultaneously relocate the aftershocks of the 1966 earthquake (Eaton et al., 1970)
113 together with the rest of the seismicity. The resulting locations are shown in Fig 1, S1c
114 and S1d. These locations resolve the fine shape of the fault plane at a level of a few tens
115 of meters. The median lateral relative error at the 95% confidence level, derived from a
116 bootstrap analysis of the fine residuals, is 0.039 km and the median vertical relative
117 error is 0.022 km (Fig. S2).

118 Most events with M < 1 (M_L is considered for events M > 3, M_D for smaller events; see
119 Uhrhammer et al., 2011) are located in the creeping section (see Supplementary Fig. S1a
120 and S1b). A cross-section at MM (Fig. 1d) indicates that some events also delineate
121 secondary oblique strands in the eastern part (see black arrows) that connect to the
122 main fault at ~10 and ~12 km depth, close to the 1966 nucleation area. Several reverse
123 and normal faulting focal mechanisms located between 10 and 15 km deep (events 3, 4,
124 5 and 6 in Fig. 1c and 1d) are aligned with those secondary strands, while those located

between 0 and 10 km deep (events 1, 2 and 7 in Fig. 1c and 1d), appear to be related to the secondary fault traces observed at the surface (black crosses, Fig. 1d).

2.2.1. Distribution of the 1966 and 2004 aftershocks

In the following analysis, we only consider earthquakes of $M \geq 1$, corresponding to the minimum magnitude of completeness of the earthquake catalog (see Supplementary Fig. S3). Fig. 2 shows the distribution of the 1966 and 2004 aftershocks within 2 months of the mainshock (in blue and red, respectively). The along strike distribution of the aftershocks is sharp and fairly similar for both events, mostly situated between 4 and 12 km deep along the Parkfield section. Distinctive seismicity patches (e.g. streaks, clusters, repeating events, Waldhauser et al., 2004; Thurber et al., 2006) outline an area devoid of earthquakes between 6-9 km deep, corresponding to the main locked patch of the fault that broke in the 1966 and 2004 events (dashed lines in Fig. 2b, Harris and Segall, 1987). The 1966 and 2004 aftershock sequences are similarly distributed, especially near GH-CH where two distinct patches of seismicity, at ~5 km and ~10 km depth, are superimposed (Fig. 2b), suggesting that the same main fault strand has been activated during the two earthquakes. A high concentration of number of aftershocks (including all $M \geq 4$ events) and cumulative moment release are observed near the rupture tips of the 1966 and 2004 earthquakes (Fig. 2a, b; Fig. 3a, b).

We note that in the northwestern part of the Parkfield section, the 1966 aftershocks tend to deviate further to the northeast away from the San Andreas fault trace (blue dots in map view on Fig. 2a). This deviation is also observed in the original absolute locations and might be due to the poor station coverage in the northwestern part of the 1966 rupture zone (Eaton et al., 1970). However, few events are concerned and our relocations are in good agreement with previous studies in the southeastern part of the

150 Parkfield section, where most of the seismicity is localized (Fig.2; e.g., Thurber et al.,
151 2006; Waldhauser and Schaff, 2008). More generally, less than 20 permanent and
152 temporary stations recorded aftershock activity following the 1966 earthquake, with
153 several periods of interrupted service (Eaton et al., 1970). This likely explains why the
154 aftershock activity and the cumulative seismic moment release shown in Figure 3 are
155 much lower for the 1966 sequence compared to the one in 2004.
156
157 *2.2.2. Interseismic periods 1969-2004 and 2005-2015*
158 We choose to represent in Fig. 2 only the best (i.e., correlation based) relocations (gray
159 dots) for the two interseismic periods from 1984–2004 and 2005–2015 for a fine-scale
160 representation of the geometrical features (see Supplementary Fig. S1 for the entire
161 relocated catalog). The interseismic seismicity distribution is remarkably similar to the
162 co- and postseismic distributions. Figure 3 shows along strike cross sections of the
163 earthquake density and cumulative seismic moment released within 2 months after the
164 1966 and 2004 Parkfield earthquakes (Fig. 3a and 3b, respectively), and during the
165 1984–2004 and 2005–2015 interseismic periods (Fig. 3c and 3d, respectively). Density
166 contour lines point out five, possibly six, persistent kilometer scale seismicity patches
167 during the interseismic periods (Fig. 3c and 3d). A patch of higher density is located at
168 the northern end of the Parkfield section at 4 km depth, a patch that was also activated
169 by aftershocks of the 2004 event (Fig. 3b).
170 The interseismic, cumulative moment release maps allow us to distinguish other patches
171 which are lining up at 4-6 km and ~10 km depth (Fig. 3c and 3d), again in good
172 agreement with patches that were active during the 1966 and 2004 post seismic periods
173 (Fig. 3a and 3b).
174

175 *2.2.3. 3D fault geometry*

176 We determine the three-dimensional fault geometry by applying a principal component
177 analysis to all events within 3 x 3 km wide boxes (in map view), stepping at 1 km
178 intervals along the fault trace. For each box, we calculate strike and dip of the plane that
179 minimizes the distance between hypocenters and fault surface during each of two
180 interseismic periods (1984-2004 and 2005-2015) in an attempt to capture the long-
181 term signature of the fault geometry (Fig. 2c). For simplicity, we assume, in each box, a
182 constant dip of the calculated plane. The calculated strike and dip values are presented
183 in Fig. 2c, while an animated view of the data and the combination of the best fitting
184 planes is shown in Supplementary Fig. S6.

185 The strike measurements show that the strike along the mainshock rupture zone, which
186 includes the stuck patch, is fairly constant, while it deviates from that trend at both ends:
187 the strongest deviations range from N125°E to N150°E (at MM and GH), consistent with
188 surface measurements (see black line in Fig. 2c), albeit with fluctuating amplitudes. The
189 overall strike variations are also in good agreement with focal mechanisms derived by
190 Hardebeck (2010; Supplementary Fig. S7). Figure 2d shows the standard deviations of
191 the seismicity from the best fitting planes for each interseismic periods, characterizing
192 the normal distance of the events from the best fitting planes (see also Supplementary
193 Fig. S4 and S5 for detailed event distribution). It confirms that MM and GH-CH are
194 characterized by greater deviations of hypocenters from the plane (400-500 m),
195 suggesting a wider off-fault deformation zone, compared to the Parkfield section (100-
196 200m). The systematic variation in strike along the fault indicates a twist in the fault
197 plane along a vertical axis.

198 Furthermore, the fault dip varies steadily from northeast dipping in the north to
199 southwest dipping in the south, indicating a twist in the fault plane along a horizontal

200 axis (Fig. 2c; e.g. Kim et al., 2016). The 3D fault geometry of the San Andreas fault at
201 Parkfield can thus be best described as a helicoid (Supplementary Fig. S6). The change in
202 fault dip from northwest to southeast can also be observed in the original NCSN
203 locations, as well as the 3D grid-search absolute locations, indicating that the twist is not
204 an artifact of the relocation procedure or the model used to locate the events (see
205 Supplementary Fig. S8).
206 Because the seismicity patches are well defined and aligned, we used the principal
207 component analysis to minimize the orthogonal hypocenter distances to a single fault
208 plane in each box (Supplementary Fig. S4). However, we also tried to investigate the
209 possibility of multiple fault strands or variations of the fault dip at depth below and
210 above 7 km (i.e. the limit between the main patches of seismicity; see Supplementary
211 Fig. S4). The resulting fault planes were poorly constrained, especially the dip values,
212 because their fits were mostly controlled by single sub-horizontal streaks, rather than
213 events well distributed on a plane in three-dimensional space. Estimating an orientation
214 by fitting one single plane in each box tend to smooth local irregularities that might be
215 due to multiple fault strands at depth. Event distributions away from the fault planes
216 (Supplementary Fig. S5) show that the Parkfield section is mainly characterized by a
217 clear and sharp single strand of ~100m wide. Secondary peaks, indicating possible
218 oblique secondary strands, are observed around MM and GH-CH. Therefore, our
219 approach cannot describe in detail the complexity of the damage zone around the fault
220 core, but it allows us to highlight significant discontinuities with great confidence.
221
222 **3. Numerical model of the effect of a strong stuck patch on fault geometry**
223 The creeping section is known from studies at SAFOD to be very weak, with a friction
224 coefficient $\mu \sim 0.15$ due to the presence of weak phyllosilicates in the fault zone (i.e.

225 saponite at shallower depth, Carpenter et al., 2015; Lockner et al., 2011, to talc below 3
226 km deep, Moore et al., 2016). They appear to be produced by reaction between the
227 serpentinite of the Coast Ranges ophiolite and the silicious rocks of the Salinian block
228 (Moore and Lockner, 2013) – a geologic context that is only present along the creeping
229 section (Allen, 1968; Irwin and Barnes, 1975). On the other hand, the stuck patch at
230 Parkfield cannot be lined with weak phyllosilicates because they are velocity
231 strengthening and will not facilitate seismic instability. The only possible materials that
232 can be velocity weakening and exhibit the frictional strength of the stuck patch in this
233 area are granite, antigorite or lizardite forms of serpentinite (Moore and Rymer, 2007).
234 These all have high strength with friction coefficients between 0.5-0.75. Thus, the
235 seismogenic stuck patch has a higher friction coefficient than the surrounding creeping
236 segment and thus can sustain greater shear stress than the stress-drops observed in
237 Parkfield earthquakes (on the order of ~1 MPa). Since the earthquakes do not relieve all
238 the stresses on the stuck patch, there must be a permanent torque produced by that
239 high-stress patch surrounded by low stress regions. As a result, over time periods longer
240 than the seismic cycle, slow inelastic deformation will occur in response to this torque
241 and the twist in the fault plane will develop.
242 In the following section, we present a numerical model that supports the above idea.
243 Rather than simulate the entire process of accumulating torque and inelastic
244 deformations, we focus on showing that a high-friction patch embedded in a low-friction
245 fault plane, representing the stuck patch situation, is able to generate deformations that
246 are consistent with the proposed helicoidal twisting of the fault plane.
247
248 *3.1 Model setup*

We use PyLith, a portable, scalable finite element software for simulation of crustal deformation and earthquake faulting (Aagaard et al., 2016, 2013), to simulate the deformation of linear elastic crust containing a straight strike-slip fault with heterogeneous frictional strengths. The model domain, covering an area 40 × 162 km wide and 21 km-thick (Fig. 4a), is discretized into hexahedral linear elements with edge length of 1 to 1.5 km. Density of the crust is assumed to be 2500 kg/m^3 and Vs and Vp to be 3 and 5.2915 km/s. These values are equivalent to shear and bulk modulus of 22.5 and 55 GPa, respectively. Completely contained within the crust, the modeled zero-thickness fault plane is 90 km long and 20 km tall, going through the center of the domain parallel to the longest edge of the domain. The creeping section is represented by a low-friction section with a uniform friction coefficient of 0.1 and a cohesion of 2 MPa ("creeping fault plane" in Fig. 4a). The stuck patch is modeled as a simplified rectangular zone of 20 × 5 km ("high friction patch" in Fig. 4; Harris and Segall, 1987). It has a uniform friction coefficient of 0.6 and a cohesion of 2 MPa. The fault section that broke during the 1857 earthquake ("high-friction fault plane" in Fig. 4), is considered to have the same friction coefficient and cohesion as the stuck patch. All the fault sections are allowed to slip because we model fault behaviors for a time period corresponding to multiple earthquake cycles, over which no part of the Parkfield section would remain completely locked.

Right-lateral motion at a rate of 2 cm/yr on two fault-parallel domain boundaries (relative on-fault slip rate of 4 cm/yr) with the normal component of velocity (v_x) set to be zero and the vertical component (v_z) free (Fig. 4b). On the fault-perpendicular sides, a simple-shear velocity field is applied such that the strike-parallel component varies between +2 and −2 cm/yr linearly with distance across the fault. The fault perpendicular component is set to be zero and the vertical component is free on these boundaries. The

bottom boundary is a free-slip surface. The top boundary is a free surface with zero traction. The effect of gravity is considered and the initial stress is set to be lithostatic. We get fault displacements and stresses as a response to incrementally increasing amounts of boundary displacements. Although we apply velocities to generate strike-slip kinematics, the velocity boundary conditions are simply a way of increasing strike-slip motions incrementally at each time step. Our models simulate only linear elastic behaviors of rocks and does not directly show rate-dependent effects. Nonetheless, the correspondence principle (e.g., Sec. 2.5.7, LeMaitre, 2001) ensure the relevance to permanent helicoidal twisting of the Parkfield section. According to this principle, strain rate field in a linear viscoelastic model would be equivalent to elastic strain field in the corresponding linear elastic model under the same boundary conditions. So, we can view our model's strain field as a strain rate field for long term deformation.

3.2. *Results*

Figure 5 presents the northeastern displacements on the fault plane when the high-friction patch and the upper 2 km of the high-friction plane started slipping after 112 m of cumulative displacement (Fig. 5a and 5c). After an unspecifiable number of earthquake cycles, slip would accumulate on the high-friction patch as well. Thus, we also look at the northeastern displacements when the entire high-friction patch as well as the upper 5 km of the high-friction plane has slipped after 160 m of boundary displacement (Fig. 5b and 5d). Relative to the state in Fig. 5a and 5c, northeastern displacements have increased at the northern tip and more at the southern tip of the patch. A major warp of the fault plane occurs at the northern tip of the high-friction patch, corresponding to MM, with northeastern displacements > 1 m along a zone approximately 10 km long (Fig. 5a and 5c). We note also that a section of the fault

situated in the southern tip of the stuck patch is slightly displaced toward the southwest when most of the high-friction patch is locked (Fig. 5a and 5c), accentuating the general warp of the fault plane. When the high friction patch starts to slip, the whole section is progressively shifted toward the northeast, but the general warping of the fault plane is still preserved (figure 5b and 5d). An animated view of the model is available in the Supplementary material (see Supplementary Fig. S9).

Cross sections in Fig. 6 show the deformation of the San Andreas Fault plane at specific locations along the model (Fig. 6a) after the stuck patch has been fully mobilized (i.e., the stage in Fig. 5b and 5d). The vertical cross-section at MM (Fig. 6b) indicates a northeastern displacement of the fault plane from its original location near the surface (hence a southwest dipping fault). Most of the deformation diffused in the crustal medium is fairly symmetrical relative to the fault plane. It seems to root at the base of the stuck patch and to widen towards the surface in a flower-like structure. The deformation is less pronounced at the southern tip of the stuck patch (i.e., GH, Fig. 6c). Yet, we can distinguish a slight deflection of the fault plane, which is displaced toward the northeast in the shallower and deeper part of the model (i.e. the creeping zones) and less so in an area that corresponds to the stuck patch. Thus, the dip of the fault plane changes with depth (i.e. toward the southwest, northeast and southwest). Figure 6d is a horizontal cross-section situated at 7.5 km depth, crossing through the creeping zones and the stuck patch (see Fig. 6a). It highlights the variation of the fault strike (grey dotted line) compared to a referenced linear fault direction (black dotted line), in the same way as in Fig. 2d. As shown in Fig. 5, the fault plane is mostly deformed toward the northeast at MM and GH, and much less so in the southern half part of the stuck patch. The strike variations within the stuck patch are consistent with the clockwise rotation of the stuck patch inferred from the seismic data (Fig. 2c, 2d).

Figure 7 provides additional information on on-fault stress distribution at two stages: after 112m of displacement (Fig. 7a), the maximum shear stress (~100 MPa) occurs at the left (northwestern) tip and corners of the rectangular stuck patch (corresponding to MM), which begins to slip. At this point, slip along the stuck patch, which is meant to represent cumulative slip from repeated earthquakes, is about 30 cm with a stress drop of ~ 1 MPa, which is regained in ~ 30 yrs. Yet, after 160 m of cumulative displacement, stress remains at about 100 MPa throughout the seismic cycles, even after the high-friction patch has slipped (Fig. 7b). Thus, slow anelastic processes can produce permanent deformation of the same type as the elastic ones shown in Fig 5. This result indicates that the high-friction patch can uphold a higher level of stress than the surrounding creeping section permanently, i.e., over a long time period corresponding to many earthquake cycles. In both states, accumulating slip on the creeping section generates high shear stress near the clamped bottom edge of the fault plane. Likewise, shear stress is concentrated right beneath the slipping region on the high-friction section, southeast of the patch (Fig. 7b). Profiles of shear and normal stresses (σ_{xy} and σ_{xx}, respectively) are shown in Supplementary Fig. S10. Along dip, the shear stress increases on the stuck patch relative to the surrounding creeping regions and higher stress concentrations are localized at the lower part of the stuck patch. Along strike, the variation of shear and normal stresses are consistent with compression at the left tip (MM) and extension at the right tip (GH-CH) of the stuck patch, resulting in clockwise rotation.

4. Discussion

4.1. Progressive deformation of the San Andreas fault over the long-term.

4.1.1. Shear stress and friction contrast at the origin of the twist

Our observational results show that the San Andreas fault plane within the rupture region of the recent ~M6 events has been deformed into a helicoidal surface that extends from the compressional bend at MM in the north to the extensional jog near GH in the south (Fig. 2c and Supplementary Fig. S6). It connects the northern part of the fault to the Cholame section in the south through a ~ 2 km wide step. By incorporating changes in fault-slip behavior at depth, our numerical model (Fig. 6) reproduces this twist and thus the variation of the fault strike (Fig. 2d, 6d) and fault dip (Fig. 2d, 6b, 6c) deduced from the seismicity analysis. The stuck patch is stronger than the surrounding creeping areas by a factor of ~4 (see section 3). The contrasting high right-lateral shear stresses on the patch will induce a torque that will bend the stuck section of the fault clockwise, as shown in Fig. 8a (map view). Because the shear stresses increase with depth, another torque increases the clockwise bending with depth (Fig. 8b). In our numerical model, the increase in shear stress from the surface to 10 km depth is about 30 MPa in the creeping section away from the stuck patch (Fig. 7a, b). However, a much stronger torque is resulted, about 120 MPa over the same vertical distance, through the stuck patch (Fig. 7b). This result shows how the assumed contrast in frictional strength can be responsible for the torques localized around the stuck patch. The two mechanisms in Fig. 8a and Fig. 8b would produce the helicoidal fault geometry that we observe (Fig. 8c). This deformed section acts like a hinge and gate, with the hinge in the north marked by the compressional bend at its onset (MM in pink, fig. 8c), and the open end of the gate to the south, where it is accommodated by the extensional jog (GH-CH in blue, fig. 8c). This suggests that the geometrical complexities at the ends of the stuck patch result from the contrast of strength of the stuck patch with the surrounding creeping section of the fault.

4.1.2. Formation and evolution of geometrical complexities and secondary structures.

One hypothesis would consider that the geometrical complexities are inherited structures formed before the presence of the stuck patch in the geologic evolution of the San Andreas fault. They would correspond to ancient relay zones between fault segments, where many WNW-ESE long-term secondary structures (Fig. 1c) would be connected to the main San Andreas Fault. As such they could play an important role in the fault structure and the rupture development of ~M6 Parkfield earthquakes. They would contribute to control the extent of the rupture, acting as structural barriers (e.g., Biasi and Wesnousky, 2017; Manighetti et al., 2007; Stirling et al., 1996) and places where stress concentrations might also favor rupture initiation (e.g., Aki, 1979; Barka and Kadinsky-Cade, 1988; Manighetti et al., 2015; Shaw, 2006). The secondary structures are possibly oblique thrusts and folds formed in a transpressive regime during the southern propagation of the San Andreas Fault (e.g. Perrin et al., 2016; Titus et al., 2011 and references therein). Their obliquity varies depending on the distance from the main San Andreas Fault (Titus et al., 2011) and some of them could be still potentially active (ex: the 1983, Mw 6.2 Coalinga thrust earthquake, Stein and King, 1984 and 1985, Mw 6.1 Kettleman Hills thrust earthquake, Ekström et al., 1992). The diffuse seismicity around Middle Mountain (Fig. 1, 2, S1, S4 and S5) might be explained by the presence of these secondary faults in the crustal medium surrounding the main San Andreas Fault. Yet, it seems unlikely that the presence of the stuck patch randomly coincides or results from the presence of the structural complexities. The San Andreas fault is a large cumulative slip fault with a very smooth (i.e., linear) surface fault trace along the central section (Wesnousky, 1988), except at the tips of the Parkfield section. Thus, it is necessary to find another mechanism responsible for the local twist of the

fault plane. We propose a second, more likely, hypothesis: the local structural complexities were lately formed by the torque of the fault plane due to the presence of a locked fault patch surrounded by creeping zones at depth. Thus, secondary geological fault traces at MM and GH-CH should be considered in the common view of the active fault traces in California. They reflect the stress concentrations at the tip of the stuck patch at depth but can also enhance them. The geometrical complexities are marked by a wider distribution of the seismicity (Fig. 2d and Supplementary Fig. S4 and S5), associated with a deflection of the San Andreas fault plane (Fig. 8 and Supplementary Fig. S6). Finally, the flower structure shape highlighted in our model (Fig. 6b) is in good agreement with the development of secondary structures at depth that widen towards the surface (Fig. 1d and Supplementary Fig. S6).

4.1.3. Interpretations and numerical modeling of the twist at Parkfield: strengths and limitations

Simpson et al. (2006), using geological and geodetical observations in addition to the 2004 aftershock locations of Thurber et al. (2006), interpreted a deflection of the active San Andreas fault near GH-CH along the vertical axis in the upper ~6 km from its surface expression as the result of non-elastic behavior of upper crustal rock units. Our observation of a systematic change in fault dip along the entire Parkfield section from MM to GH-CH suggests an additional torque along the horizontal axis that causes the helicoidal nature of the three-dimensional fault plane, as shown in our model (Fig. 6). This shape is not predicted by the 2D numerical model in Simpson et al. (2006), which considers a constant, near-vertical dip at depth to obtain a warp in the fault plane with a major deflection at GH-CH, but not at MM. They suggest that the warp is due to slip in the creeping zone (including the Parkfield stuck patch), which results in inelastic

424 deformation that is not released further to the south by large events similar to the 1857
425 earthquake. Our model of the helicoidal twist is based on the long-term difference in
426 strength between persistent structures that represent stuck and creeping areas, and
427 hence does not require inelasticity with such a short time constant.
428 The high friction patch ($\mu \sim 0.6$) is velocity weakening and so exhibits an earthquake
429 cycle. It is embedded in a region of low friction ($\mu \sim 0.2$) which continuously slides in a
430 stable manner. This strength contrast will place a clockwise torque on the system which
431 by slow inelastic deformation over geologic time has twisted the fault. In this regard, our
432 numerical models serve only two purposes: i) to demonstrate that the clockwise torque
433 can arise from the assumed contrast in frictional strength along the Parkfield section
434 and ii) to show that the clockwise torque can be sustained over many earthquake cycles
435 on the high-friction patch.
436 In our model, the shear stress magnitude is significant (~100 MPa) and the
437 correspondend principle between the linear elastic and the linear viscoelastic strain
438 implies, over the long term, that our model's strain field could induce the development
439 of permanent inelastic deformation in the upper part of the crust. This deformation
440 might correspond to the secondary faults and fractures observed at surface and at depth
441 at the tips of the stuck patch. More sophisticated fault and material models would be
442 needed to investigate a causal relationship between the helicoidal twist of the stuck
443 patch and the formation of secondary structures.
444 Our model indicates lateral deformation of the San Andreas fault of 1.5 m to 2 m at MM
445 and 1.3 m to 2.5 m at GH (at surface and at depth, respectively) after 160 m of
446 cumulative slip. Considering the current total cumulative slip around Parkfield since the
447 fault initiation (i.e. ~315 km; (Crowell, 1979; Revenaugh and Reasoner, 1997 and
448 references therein), it would imply a total northeastern fault deformation of ~3 to ~4

449 km and ~2.5 to ~5 km at MM and GH, respectively. While this deformation is
450 comparable observations at GH (~2 km wide step-over at the surface), it is not the case
451 at MM. However, we note that our model has exaggerated contrast in friction strength
452 between the patch and the creeping section. Increasing the friction coefficient of the
453 creeping section to 0.2, compared to 0.1 used here, would possibly subdue the amount of
454 the northeastern fault deformation. In addition, our model does not include the
455 development of new secondary faults and fractures, which may have been created in the
456 surrounding medium to accommodate the deflection of the San Andreas fault, just like
457 the ~5 km wide zone of deformation identified at MM (see Fig. 1 and Thayer, 2006).
458 Additional minor faults might be also present but they have been possibly eroded or
459 hidden under sedimentary deposits.
460 Finally, we remind that our model is a simplified view that cannot exactly reproduce the
461 deformation pattern of the San Andreas fault at Parkfield. The results are sensitive to the
462 initial conditions (i.e. relative location of the stuck patch at depth and connection with
463 the locked section in the south). For instance, we assume a vertical initial fault dip and
464 the model does not reproduce the NE dip of the fault in the creeping section (Fig. 2c). On
465 the other hand, we are not sure that this dip is related to the torque of the fault plane
466 due to the presence of the stuck patch or rather to the initial fault dip of the San Andreas
467 fault. All these parameters were not explored in this study and need to be tested in
468 future models. Our model is used here to show that the right lateral motion and the
469 change in fault sip behavior due to the presence of the stuck patch are in good
470 agreement with the torque highlighted in our observations. The resulting stress and
471 displacement values should be used with caution.
472
473 *4.2. Impact of fault structures on the seismicity behavior and the earthquake cycle*

Our results confirm that major structural discontinuities, such as secondary reverse and normal faults, are present at the surface near the transitions between the Parkfield and creeping sections at MM, and the Parkfield and Cholame sections near GH-CH (Fig.1). Fine-scale analysis of the seismicity indicates that these structural complexities extend at depth and correlate with the vertices of the elliptical stuck patch that ruptures in M6 events (Fig. 2 and 3). It is recognized that aftershocks occur mostly at the edges of regions experiencing high coseismic slip or in areas of low coseismic slip (e.g., Mendoza and Hartzell, 1988), regardless of initial stress conditions. Along the Parkfield section, earthquake locations in both the post-seismic and interseismic periods over one and a half seismic cycles delineate the margins of the stuck patch (i.e. transition between locked and creeping areas on the fault; Fig. 2 and 3). Especially, figure 3d updates the common view of the "stationary" seismicity around the stuck patch, going through a new interseismic period, during the decade following the 2004 earthquake. Therefore, our observations indicate that the stress concentrations that surround the stuck patch and therefore the stuck patch itself are long-term permanent features controlling the rupture process.

Based on the results from our model (Fig. 7), we schematize in Fig. 9 the state of stress and seismicity distribution on the fault plane. The seismicity distribution reflects significant stress concentrations between creeping regions, which are velocity strengthening and hence frictionally stable, and the locked region (i.e. stuck patch), which is velocity weakening and hence unstable. During interseismic periods (stage 1 in Fig. 9), the stress increases on the stuck patch relative to the surrounding creeping regions and higher stress concentrations are localized at the edge of the stuck patch. The resulting stress concentrations lead to higher seismic activity at the transition between locked and creeping regions. Coseismic slip produces surrounding stress concentrations

during the postseismic period (stage 2 in Fig. 9) which also induces enhanced seismicity in that area. Then, the stress accumulates again along the locked section during the following interseismic period (stage 3 in Fig. 9), producing a similar behavior as in stage 1.

Our model shows that the long-term deformation of the fault plane is prominent at the along-strike extremities of the stuck patch (Fig. 5 and 6), leading to a concentration of stress and strain that can affect the seismic cycle. These zones also correspond to the nucleation locations of the 1934, 1966, and 2004 earthquakes (Bakun et al., 2005; Bakun and McEvilly, 1979). This behavior is also expected from results of dynamic modeling (Das and Kostrov, 1985) of rupture of an elliptical asperity, where the stress concentrations reach a maximum at the vertices of the semi-major axes of the ellipse. The rupture terminates shortly after it impinges on the velocity-strengthening region. This constitutes a stability barrier, as demonstrated by Kaneko et al. (2010). However, recent studies (Noda and Lapusta, 2013) show that some earthquake ruptures might also propagate through creeping areas that were considered to be barriers. The similarity of slip distribution of Parkfield earthquakes seems to suggest that the creeping zones stop rupture propagation at least for M6 and smaller earthquakes. The observation of logarithmically decaying afterslip sequences in the creeping section above the stuck patch following both the 1966 and 2004 earthquakes (e.g. Barbot et al., 2009; Langbein et al., 2006; Murray and Langbein, 2006; Scholz et al., 1969) is consistent with the model of Marone et al. (1991), in which a velocity strengthening region overlies a velocity weakening one.

5. Conclusions

We present a model based on geological surface observations and seismological observations at depth in which the three-dimensional structural complexities near MM and GH of the San Andreas Fault originate from the presence of a stuck patch surrounded by a creeping zone at Parkfield. The progressive helicoidal twist of the fault plane is due to a torque arising from the contrast in frictional strength between the stuck patch and the surrounding weak creeping area. The complex structures at each end of the helicoid result from the stress concentrations at these locations. They are characterized by complex reverse and normal faulting at the surface and diffuse seismicity at depth. These structural complexities are permanent features, playing an important role in stress concentrations and occurrence of M6 earthquakes at Parkfield.

Faults are laterally segmented along their traces. In the early stages of their evolution, the fault segments are separated by geometrical discontinuities possibly formed by small secondary faults and fractures As the fault grows and lengthens through time, fault segments tend to become more and more connected and the lateral discontinuities in between smoothed out (e.g. Manighetti et al., 2015 and references therein). The main strand of the San Andreas fault at Parkfield is extraordinarily smooth, as a result of its large cumulative slip (Wesnousky, 1988); the 2-km fault offset at GH-CH being a notable exception. We find that this offset is a constructive edifice resulting in the strength contrast in the fault at this locality. This example of fault roughening with slip is in contrast to the generally assumed smoothing of fully locked faults at they become more mature.

ACKNOWLEDMENTS

This work is supported by the Brinson Foundation, and the National Science Foundation (NSF-EAR #1520680). We thank A. Lomax for his help with the *NLLoc* software. We

548 thank the editor J.-P. Avouac, two anonymous reviewers and S. Barbot for their thorough
549 comments that greatly improved the manuscript. Earthquake catalog data is available at
550 http://ddrt.ldeo.columbia.edu. The DEM data (Lidar, SRTM3) have been provided by the
551 OpenTopography Facility with support from the National Science Foundation under NSF
552 Award Numbers 1226353 & 1225810. This paper is LDEO contribution 8319 and IPGP
553 contribution 4043.
554

555 **REFERENCES CITED**

556 Aagaard, B.T., Knepley, M.G., Williams, C.A., 2016. PyLith User Manual, Version 2.1.2.
557 [WWW Document]. Comput. Infrastruct. Geodyn. URL
558 http://geodynamics.org/cig/software/github/pylith/v2.1.2/pylith-
559 2.1.2_manual.pdf
560 Aagaard, B.T., Knepley, M.G., Williams, C.A., 2013. A domain decomposition approach to
561 implementing fault slip in finite-element models of quasi-static and dynamic crustal
562 deformation. J. Geophys. Res. Solid Earth 118, 3059–3079. doi:10.1002/jgrb.50217
563 Aki, K., 1979. Characterization of barriers on an earthquake fault. J. Geophys. Res. 84,
564 6140–6148.
565 Allen, C.R., 1968. The tectonic environments of seismically active and inactive areas
566 along the San Andreas fault system. Stanford Univ. Publ. Geol. Sci. 11.
567 Archuleta, R.J., Day, S.M., 1980. Dynamic rupture in a layered medium: the 1966
568 Parkfield earthquake. Bull. Seismol. Soc. Am. 70, 671–689.
569 Bakun, W.H., Aagaard, B., Dost, B., Ellsworth, W.L., Hardebeck, J.L., Harris, R.A., Ji, C.,
570 Johnston, M.J.S., Langbein, J., Lienkaemper, J.J., Michael, A.J., Murray, J.R., Nadeau,
571 R.M., Reasenberg, P.A., Reichle, M.S., Roeloffs, E.A., Shakal, A., Simpson, R.W.,
572 Waldhauser, F., 2005. Implications for prediction and hazard assessment from the

573 2004 Parkfield earthquake. Nature 437, 969–974. doi:10.1038/nature04067
574 Bakun, W.H., McEvilly, T. V., 1979. Earthquakes near Parkfield, California: Comparing the
575 1934 and 1966 Sequences. Science 205, 1375–1377.
576 doi:10.1126/science.205.4413.1375
577 Barbot, S., Fialko, Y., Bock, Y., 2009. Postseismic deformation due to the Mw 6.0 2004
578 Parkfield earthquake: Stress-driven creep on a fault with spatially variable rate-
579 and-state friction parameters. J. Geophys. Res. Solid Earth 114, 0–26.
580 doi:10.1029/2008JB005748
581 Barbot, S., Lapusta, N., Avouac, J.-P., 2012. Under the Hood of the Earthquake Machine :
582 Toward Predictive Modeling. Science (80-.). 336, 707–710.
583 doi:10.1126/science.1218796
584 Barka, A., Kadinsky-Cade, K., 1988. Strike-slip fault geometry in Turkey. Tectonics 7,
585 663–684. doi:10.1029/TC007i003p00663
586 Biasi, G.P., Wesnousky, S.G., 2017. Bends and Ends of Surface Ruptures. Bull. Seismol.
587 Soc. Am. 1–18. doi:10.1785/0120160292
588 Brown, R.D.J., Vedder, J.G., Wallace, R.E., Roth, E.F., Yerkes, R.F., Castle, R.O., Waananen,
589 A.O., Page, R.W., Eaton, J.P., 1967. The Parkfield-Cholame, California, earthquakes of
590 June-August 1966 - surface geologic effects, water-resources aspects, and
591 preliminary seismic data. U.S. Geol. Surv. Prof. Pap. 66.
592 Bruhat, L., Barbot, S., Avouac, J.P., 2011. Evidence for postseismic deformation of the
593 lower crust following the 2004 Mw6.0 Parkfield earthquake. J. Geophys. Res. Solid
594 Earth 116, 1–10. doi:10.1029/2010JB008073
595 Carpenter, B.M., Saffer, D.M., Marone, C., 2015. Frictional properties of the active San
596 Andreas Fault at SAFOD: Implications for fault strength and slip behavior. J.
597 Geophys. Res. Solid Earth 120, 5273–5289. doi:10.1002/2015JB011963

598 Crowell, J.C., 1979. The San Andreas fault system through time. J. Geol. Soc. London. 136,
599 293–302. doi:10.1144/gsjgs.136.3.0293
600 Das, S., Kostrov, B. V., 1985. An elliptical asperity in shear: fracture process and seismic
601 radiation. Geophys. J. Int. 80, 725–742. doi:10.1111/j.1365-246X.1985.tb05121.x
602 Eaton, J.P., O'Neill, M.E., Murdock, J.N., 1970. Aftershocks of the 1966 Parkfield-Cholame,
603 California, earthquake: A detailed study. Bull. Seismol. Soc. Am. 60, 1151–1197.
604 Ekström, G., Stein, R.S., Eaton, J.P., Eberhart-Phillips, D., 1992. Seismicity and geometry of
605 a 110-km-long blind thrust fault 2. Synthesis of the 1982–1985 California
606 Earthquake Sequence. J. Geophys. Res. 97, 4843–4864. doi:10.1029/91JB02847
607 Hardebeck, J.L., 2010. Seismotectonics and fault structure of the California Central Coast.
608 Bull. Seismol. Soc. Am. 100, 1031–1050. doi:10.1785/0120090307
609 Harris, R.A., Segall, P., 1987. Detection of a Locked Zone at Depth on the Parkfield,
610 California, Segment of the San Andreas Fault. J. Geophys. Res. 92, 7945–7962.
611 doi:10.1029/JB092iB08p07945
612 Irwin, W.P., Barnes, I., 1975. Effects of geological structure and metamorphic fluids on
613 seismic behavior of the San Andreas fault system in central and northern California.
614 Geology 3, 713–716.
615 Johanson, I.A., Fielding, E.J., Rolandone, F., Bürgmann, R., 2006. Coseismic and
616 postseismic slip of the 2004 Parkfield earthquake from space-geodetic data. Bull.
617 Seismol. Soc. Am. 96, 269–282. doi:10.1785/0120050818
618 Kaneko, Y., Avouac, J.-P., Lapusta, N., 2010. Towards inferring earthquake patterns from
619 geodetic observations of interseismic coupling. Nat. Geosci. 3, 363–369.
620 doi:10.1038/ngeo843
621 Kim, W., Hong, T.-K., Lee, J., Taira, T., 2016. Seismicity and fault geometry of the San
622 Andreas fault around Parkfield, California and their implications. Tectonophysics

677–678, 34–44. doi:10.1016/j.tecto.2016.03.038

Langbein, J., Borcherdt, R., Dreger, D., Fletcher, J., Hardebeck, J.L., Hellweg, M., Ji, C., Johnston, M., Murray, J.R., Nadeau, R., Rymer, M.J., Treiman, J. a., 2005. Preliminary Report on the 28 September 2004, M 6.0 Parkfield, California Earthquake. Seismol. Res. Lett. 76, 10–26. doi:10.1785/gssrl.76.1.10

Langbein, J., Murray, J.R., Snyder, H.A., 2006. Coseismic and initial postseismic deformation from the 2004 Parkfield, California, earthquake, observed by global positioning system, electronic distance meter, creepmeters, and borehole strainmeters. Bull. Seismol. Soc. Am. 96, 304–320. doi:10.1785/0120050823

LeMaitre, J., 2001. Handbook of Materials Behavior Models. Academic press.

Lindh, A.G., Boore, D.M., 1981. Control of Rupture by Fault Geometry During the 1966 Parkfield Earthquake. Bull. Seismol. Soc. Am. 71, 95–116.

Lockner, D.A., Morrow, C., Moore, D., Hickman, S., 2011. Low strength of deep San Andreas fault gouge from SAFOD core. Nature 472, 82–85. doi:10.1038/nature09927

Lomax, A., Virieux, J., Volant, P., Berge, C., 2000. Probabilistic earthquake location in 3D and layered models: Introduction of a Metropolis-Gibbs method and comparison with linear locations, in: Thurber, C.H., Rabinowitz, N. (Eds.), Advances in Seismic Event Location. Amsterdam, pp. 101–134.

Manighetti, I., Campillo, M., Bouley, S., Cotton, F., 2007. Earthquake scaling, fault segmentation, and structural maturity. Earth Planet. Sci. Lett. 253, 429–438. doi:10.1016/j.epsl.2006.11.004

Manighetti, I., Caulet, C., De Barros, D., Perrin, C., Cappa, F., Gaudemer, Y., 2015. Generic along-strike segmentation of Afar normal faults, East Africa: Implications on fault growth and stress heterogeneity on seismogenic fault planes. Geochem. Geophys.

Geosyst. 16, 443–467. doi:10.1002/2014GC005691.Received

Marone, C.J., Scholz, C.H., Bilham, R., 1991. On the mechanics of earthquake afterslip. J. Geophys. Res. 96, 8441. doi:10.1029/91JB00275

McEvilly, T. V., Bakun, W.H., Casaday, K.B., 1967. The Parkfield, California, earthquakes of 1966 57, 1221–1244.

Mendoza, C., Hartzell, S.H., 1988. Aftershock patterns and main shock faulting. Bull. Seismol. Soc. Am. 78, 1438–1449.

Moore, D.E., Lockner, D.A., 2013. Chemical controls on fault behavior: Weakening of serpentinite sheared against quartz-bearing rocks and its significance for fault creep in the San Andreas system. J. Geophys. Res. Solid Earth 118, 2558–2570. doi:10.1002/jgrb.50140

Moore, D.E., Lockner, D.A., Hickman, S., 2016. Hydrothermal frictional strengths of rock and mineral samples relevant to the creeping section of the San Andreas Fault. J. Struct. Geol. 89, 153–167. doi:10.1016/j.jsg.2016.06.005

Moore, D.E., Rymer, M.J., 2007. Talc-bearing serpentinite and the creeping section of the San Andreas fault. Nature 448, 795–797. doi:10.1038/nature06064

Murray, J., Langbein, J., 2006. Slip on the San Andreas fault at Parkfield, California, over two earthquake cycles, and the implications for seismic hazard. Bull. Seismol. Soc. Am. 96, 283–303. doi:10.1785/0120050820

Noda, H., Lapusta, N., 2013. Stable creeping fault segments can become destructive as a result of dynamic weakening. Nature 493, 518–521. doi:10.1038/nature11703

Perrin, C., Manighetti, I., Gaudemer, Y., 2016. Off-fault tip splay networks: A genetic and generic property of faults indicative of their long-term propagation. Comptes Rendus Geosci. 348, 52–60. doi:10.1016/j.crte.2015.05.002

Revenaugh, J., Reasoner, C., 1997. Cumulative offset of the San Andreas fault in central

673 California: A seismic approach. Geology 25, 123–126. doi:10.1130/0091-
674 7613(1997)025<0123:COOTSA>2.3.CO;2
675 Rymer, M.J., Tinsley, J.C., Treiman, J.A., Arrowsmith, J.R., Ciahan, K.B., Rosinski, A.M.,
676 Bryant, W.A., Snyder, H.A., Fuis, G.S., Toké, N.A., Bawden, G.W., 2006. Surface fault
677 slip associated with the 2004 Parkfield, California, earthquake. Bull. Seismol. Soc.
678 Am. 96, 11–27. doi:10.1785/0120050830
679 Schaff, D.P., Waldhauser, F., 2005. Waveform cross-correlation-based differential travel-
680 time measurements at the northern California seismic network. Bull. Seismol. Soc.
681 Am. 95, 2446–2461. doi:10.1785/0120040221
682 Scholz, C.H., Wyss, M., Smith, S.W., 1969. Seismic and aseismic slip on the San Andreas
683 Fault. J. Geophys. Res. 74, 2049–2069. doi:10.1029/JB074i008p02049
684 Segall, P., Du, Y., 1993. How similar were the 1934 and 1966 Parkfield earthquakes? J.
685 Geophys. Res. 98, 4527-4538 (doi: 10.1029/92JB02408). doi:10.1029/92JB02408
686 Shaw, B.E., 2006. Initiation propagation and termination of elastodynamic ruptures
687 associated with segmentation of faults and shaking hazard. J. Geophys. Res. 111,
688 B08302. doi:10.1029/2005JB004093
689 Simpson, R.W., Barall, M., Langbein, J., Murray, J.R., Rymer, M.J., 2006. San Andreas fault
690 geometry in the Parkfield, California, region. Bull. Seismol. Soc. Am. 96, 28–37.
691 doi:10.1785/0120050824
692 Stein, R.S., King, G.C.P., 1984. Seismic potential revealed by surface folding: 1983
693 Coalinga, California, earthquake. Science (80-.). 224, 869–872.
694 Stirling, M.W., Wesnousky, S.G., Shimazaki, K., 1996. Fault trace complexity, cumulative
695 slip, and the shape of the magnitude-frequency distribution for strike-slip faults: a
696 global survey. Geophys. J. Int. 124, 833–868. doi:10.1111/j.1365-
697 246X.1996.tb05641.x

698 Thayer, M., 2006. Structural Geology of the San Andreas Fault Zone at Middle Mountain,
699 near Parkfield, Central California. Doctoral dissertation, Arizona State University.
700 Thurber, C., Zhang, H., Waldhauser, F., Hardebeck, J.L., Michael, A.J., Eberhart-Phillips, D.,
701 2006. Three-Dimensional Compressional Wavespeed Model, Earthquake
702 Relocations, and Focal Mechanisms for the Parkfield, California, Region. Bull.
703 Seismol. Soc. Am. 96, S38–S49. doi:10.1785/0120050825
704 Titus, S.J., Dyson, M., DeMets, C., Tikoff, B., Rolandone, F., Bürgmann, R., 2011. Geologic
705 versus geodetic deformation adjacent to the San Andreas fault, central California.
706 Bull. Geol. Soc. Am. 123, 794–820. doi:10.1130/B30150.1
707 U.S. Geological Survey and California Geological Survey, 2006. Quaternary fault and fold
708 database for the United States [WWW Document]. URL
709 https://earthquake.usgs.gov/hazards/qfaults/. (accessed 10.2.14).
710 Uhrhammer, R.A., Hellweg, M., Hutton, K., Lombard, P., Walters, A.W., Hauksson, E.,
711 Oppenheimer, D., 2011. California integrated seismic network (CISN) local
712 magnitude determination in California and vicinity. Bull. Seismol. Soc. Am. 101,
713 2685–2693. doi:10.1785/0120100106
714 Waldhauser, F., 2004. Streaks, multiplets, and holes: High-resolution spatio-temporal
715 behavior of Parkfield seismicity. Geophys. Res. Lett. 31, L18608.
716 doi:10.1029/2004GL020649
717 Waldhauser, F., 2001. HypoDD: A computer program to compute double-difference
718 hypocenter locations. U.S. Geol. Surv. Open File Rep. 01-113, Menlo Park. Calif. 25.
719 Waldhauser, F., Ellsworth, W.L., 2000. A Double-difference Earthquake location
720 algorithm: Method and application to the Northern Hayward Fault, California. Bull.
721 Seismol. Soc. Am. 90, 1353–1368. doi:10.1785/0120000006
722 Waldhauser, F., Schaff, D.P., 2008. Large-scale relocation of two decades of Northern

California seismicity using cross-correlation and double-difference methods. J. Geophys. Res. Solid Earth 113, 1–15. doi:10.1029/2007JB005479

Wesnousky, S.G., 1988. Seismological and structural evolution of strike-slip faults. Nature. doi:10.1038/335340a0

FIGURES CAPTIONS

Figure 1: a) Map view of central California. White triangles are the 212 stations that recorded the ~17,000 events; b) Fault map along the Parkfield section and relocated seismicity (red dots) from 1966 to 2015. Black circles are events with M ≥ 4. White stars are the 1966 and 2004 epicenters. Fault traces are shown on SRTM3 topography illuminated from the southwest. Blue lines are quaternary fault traces from the (U.S. Geological Survey and California Geological Survey, 2006); black lines are additional long-term fault traces from this study and Thayer (2006) (dotted black lines when uncertain). SAF: San Andreas Fault; SJF: San Juan Fault; MM: Middle Mountain; GH: Gold Hill; CH: Cholame; c) Zoom into Middle Mountain area. Focal mechanisms (Hardebeck, 2010) showing intermediate to low-angle dipping fault motions (< 70°). d) Cross section (AA') showing the relocated seismicity from 1966 to 2015 (red dots) at Middle Mountain. Black crosses are fault traces at surface. The white star represents the 1966 hypocenter. Black arrows point possible secondary active strands at depth. Numbered focal mechanisms in c) and d) point out specific thrust (red) and normal (blue) faulting earthquakes (front projection).

Figure 2: a) Rotated map view of all surface fault traces from fig.1 (black lines) and the relocated seismicity (M ≥ 1). Blue and red dots are early aftershocks (2 months) of the

748 1966 and 2004 ~M6 earthquakes, respectively. Gray dots are background seismicity
749 (1984 to 2015; see Supplementary Fig. S1 for full catalog). Larger dots are M≥4 events
750 since 1979. White stars represent the 1966 and 2004 epicenters. MM: Middle Mountain;
751 GH: Gold Hill. b) Along-strike cross section. Same legend as in a. Circles indicate size of a
752 circular source model with a 3 MPa stress drop. Dashed dark lines are contours of the
753 interseismic slip rate in mm/yr predicted by geodetic inversion (Harris and Segall,
754 1987). c) Variation of the fault strike and dip along the Parkfield section. The mean
755 reference fault strike and dip are 139° and 90° (vertical), respectively. Solid black curve
756 represents the main San Andreas fault strike measured at surface (secondary faults not
757 included). Green and orange curves are inferred strike and dip at depth from the best
758 fitting planes for the 1984-2004 and 2004-2015 interseismic periods, respectively. Gray
759 zones are location of major complexities observed at surface near Middle Mountain and
760 Gold Hill-Cholame. d) Half standard deviation from the best fitting planes calculated in
761 each box (see also Supplementary Fig. S4 and S5) for the 1984-2004 and 2004-2015
762 interseismic periods (green and orange shaded curves, respectively).
763
764 **Figure 3**: Along-strike cross-sections showing projected earthquake density (contours,
765 counts per km^2) and cumulative seismic moment (color scale) released along the
766 Parkfield section for a) 1966 and b) 2004 aftershocks, and c) 1984-2004 and d) 2005-
767 2015 periods. White stars are 1966 and 2004 ~M6 hypocenters. Grey dashed lines are
768 coseismic slip distributions (in m) of the a) 1966 (Segall and Du, 1993) and b) 2004
769 (Bruhat et al., 2011) earthquakes. Gray zones are location of major complexities
770 observed at surface near Middle Mountain and Gold Hill-Cholame.
771

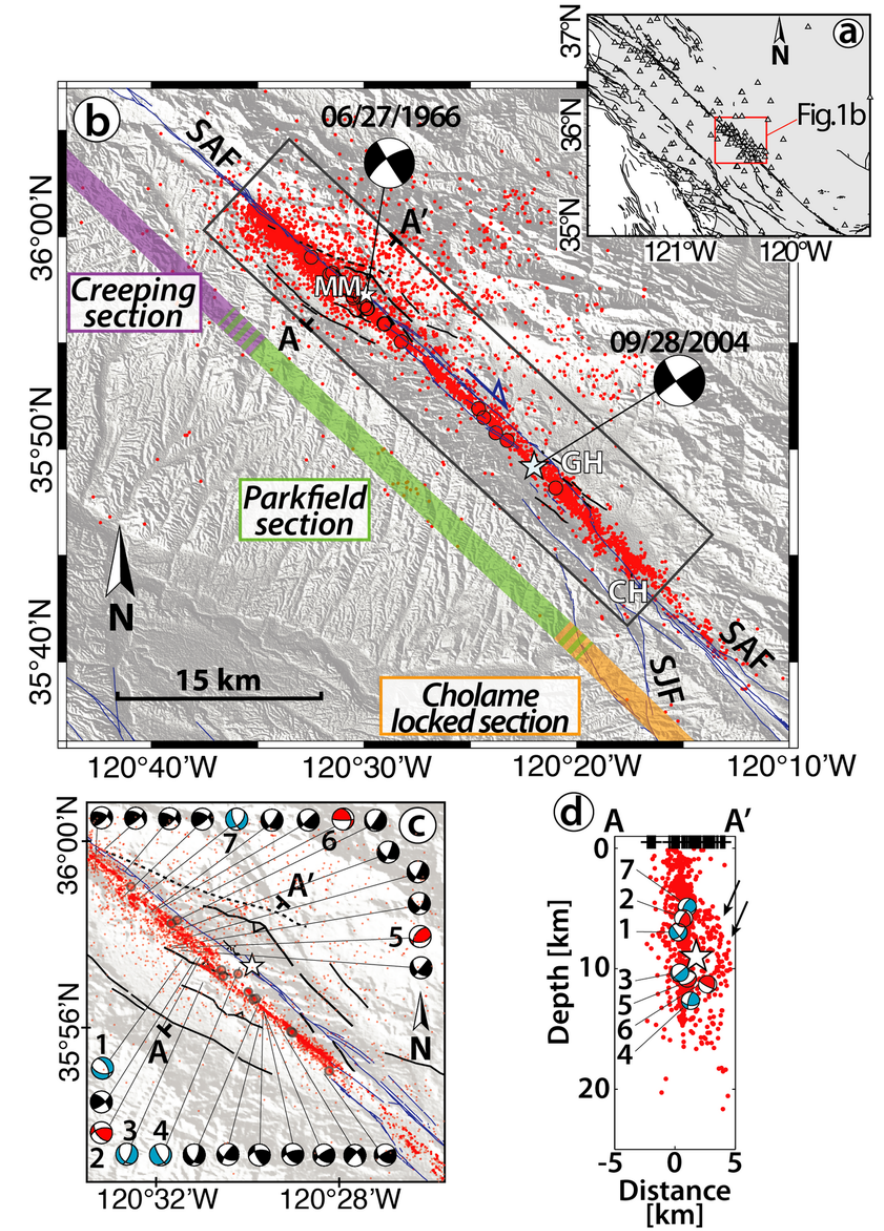
772 **Figure 4:** (a) Geometry of the model domain and the fault plane. (b) Boundary
773 conditions on the sides and the bottom as well as frictional properties on the fault plane.
774 The top surface is a free surface. The fault section of the model includes creeping
775 sections (in grey) and fully locked zone (in white; stuck patch near Parkfield and
776 Southern Cholame/Fort Tejon section).
777
778 **Figure 5:** (a) Perpendicular displacement of the fault plane toward the northeast and
779 slightly toward the southwest (top) and cumulative fault slip distribution (bottom)
780 around the stuck patch and the high-friction section outlined by the solid black
781 rectangles after 112 m of boundary displacement. (b) Same as in (a) after 160 m of
782 boundary displacement. (c) and (d) Northeast-looking view of the fault plane after 112m
783 and 160 m of boundary displacement, respectively (mesh with the slip magnitudes
784 colored in gray scale), and the central plane deformed by the northeast and southwest
785 directed displacements. The solid back rectangles outline the stuck patch and the high-
786 friction section.
787
788 **Figure 6:** (a) Locations of the two vertical cross-sections corresponding to Middle
789 Mountain (MM) and Gold Hill (GH) and one horizontal section going through the center
790 of the stuck patch at the depth of 7.5 km. (b) In-plane displacement magnitudes on the
791 MM cross-section that is displaced by the 500 times amplified in-plane displacement
792 vectors. Black squares are the original locations of the nodes on the central plane and
793 gray squares are the displaced locations of the same nodes after 60 m of boundary
794 displacement. Gray lines show the computational mesh. Thin black lines outline the
795 original rectangular shape of the cross-section. (c) Same as (b) but for the GH cross-

section. (d) Northeast displacement magnitudes plotted on the horizontal section displaced by the northeast displacement vectors. Symbols are the same as in (b).

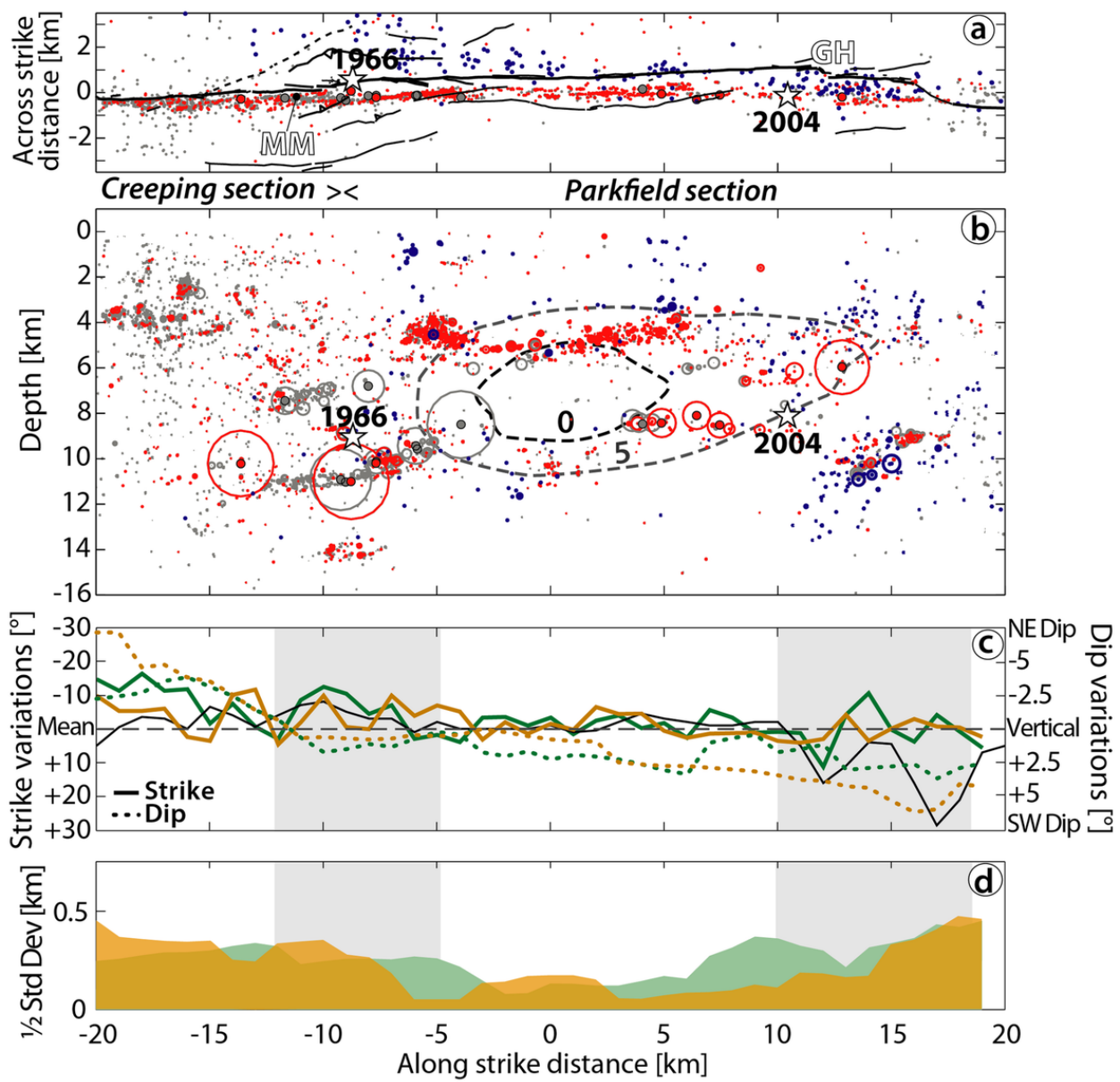
Figure 7: Along-strike shear stress map on the fault plane at two stages of the simulation (after 112 and 160 m of displacement). Note the *x* axis is into the plane and the *y* axis is pointing to the left. So, the right-lateral motion generates negative values of shear stress (σ_{xy}).

Figure 8: Schematic map view (a) and cross section (b) showing the clockwise rotation of the fault plane due to the presence of a stuck patch surrounded by a creeping zone. In (a) the size of the shear couple arrows scales with the amount of shear stress. Positive and minus signs are compressional and extensional regimes, respectively; in (b) the increasing size of dextral motion indicates increasing shearing stresses with depth and thus the clockwise torque (red arrows); c) 3D sketch synthesizing the clockwise twist into a helicoidal fault plane at Parkfield and its relation with changes in fault-slip behavior, structural discontinuities and earthquake distribution; MM: Middle Mountain; GH: Gold Hill; CH: Cholame.

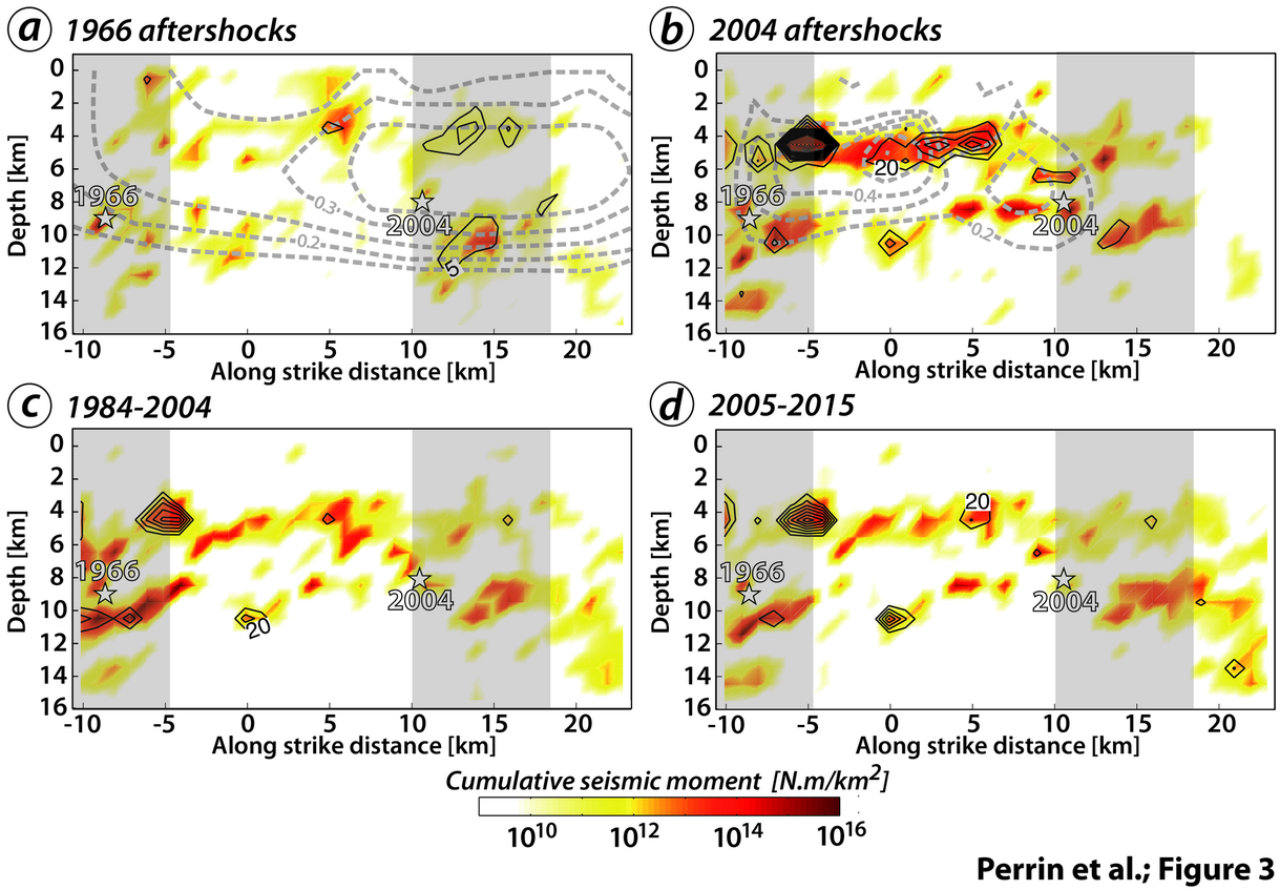
Figure 9: Sketch showing a simplified view of the Parkfield fault section and along dip distribution of stress and seismicity rates (profile AA') as predicted from a locked patch at mid-crustal depth imbedded in an otherwise creeping fault. Seismic activity is driven by the difference in the stress rate at the edge of the locked patch at every stage of the earthquake cycle.



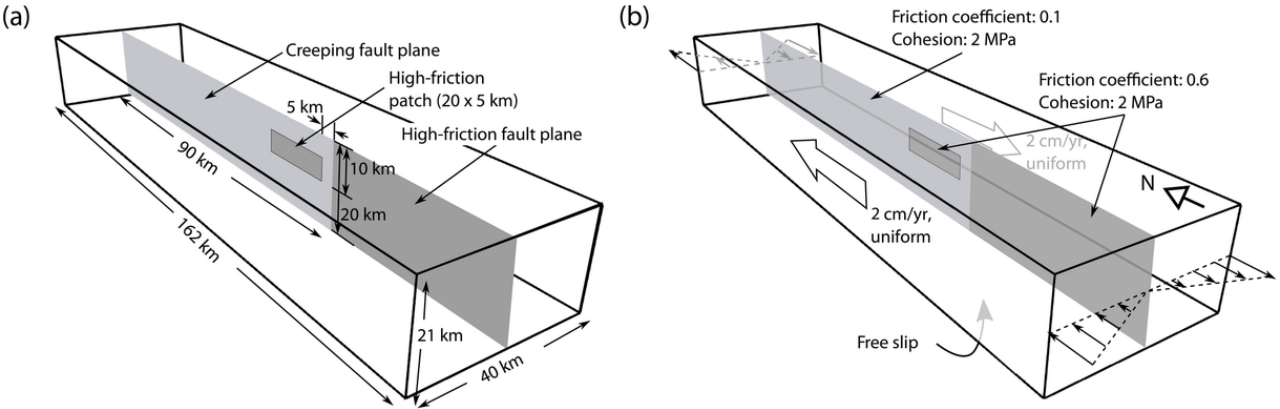
Perrin et al.; Figure 1



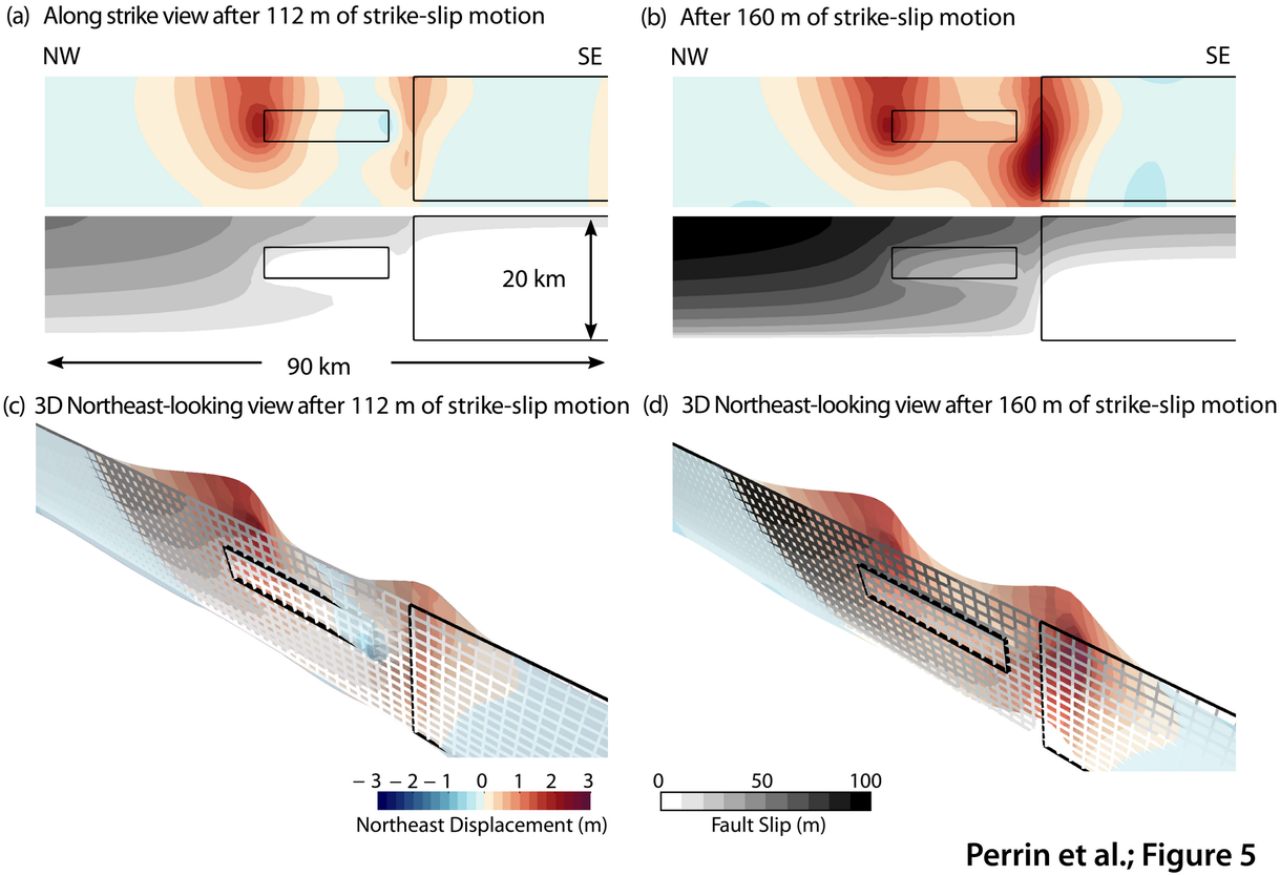
Perrin et al.; Figure 2



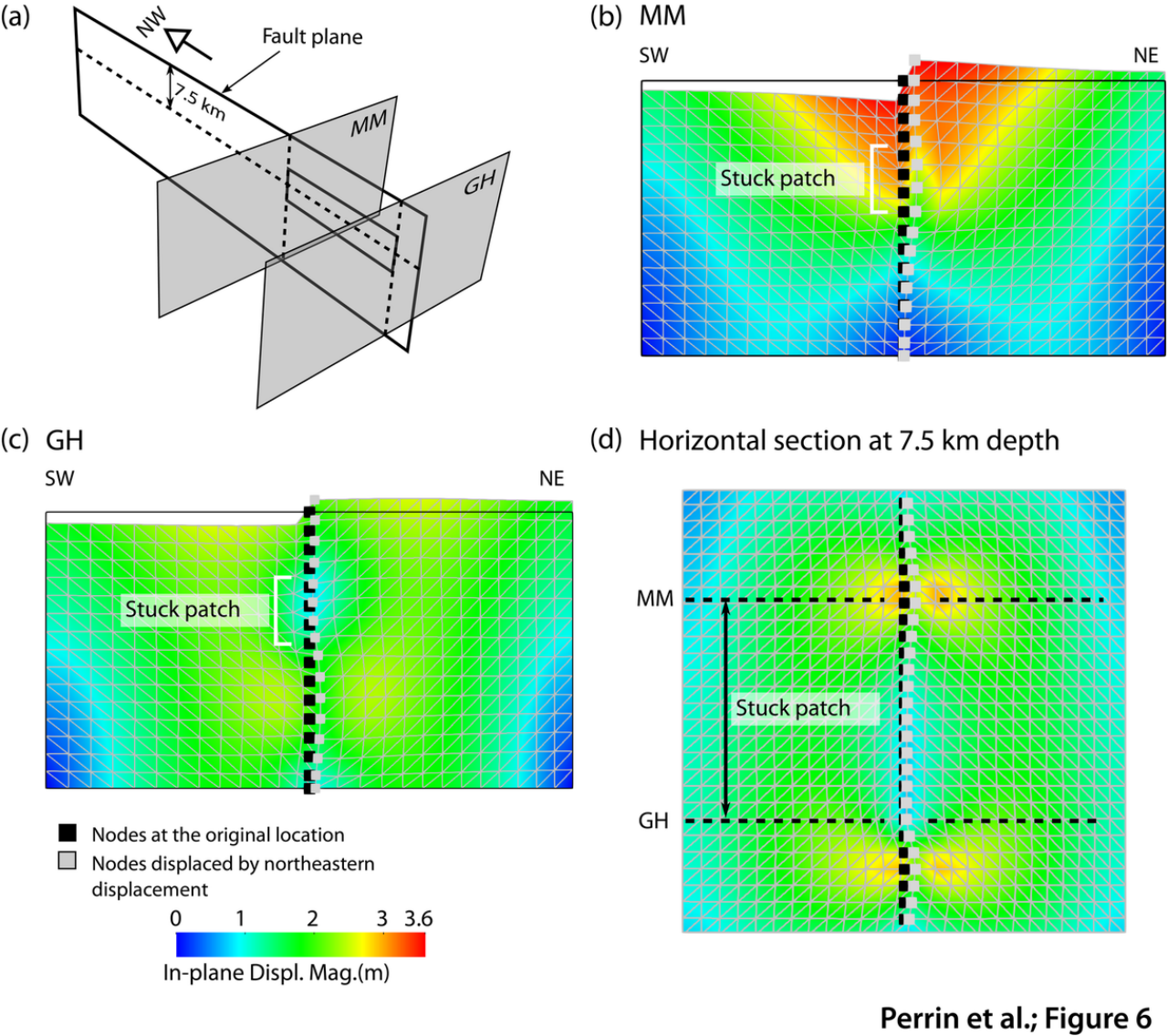
Perrin et al.; Figure 3



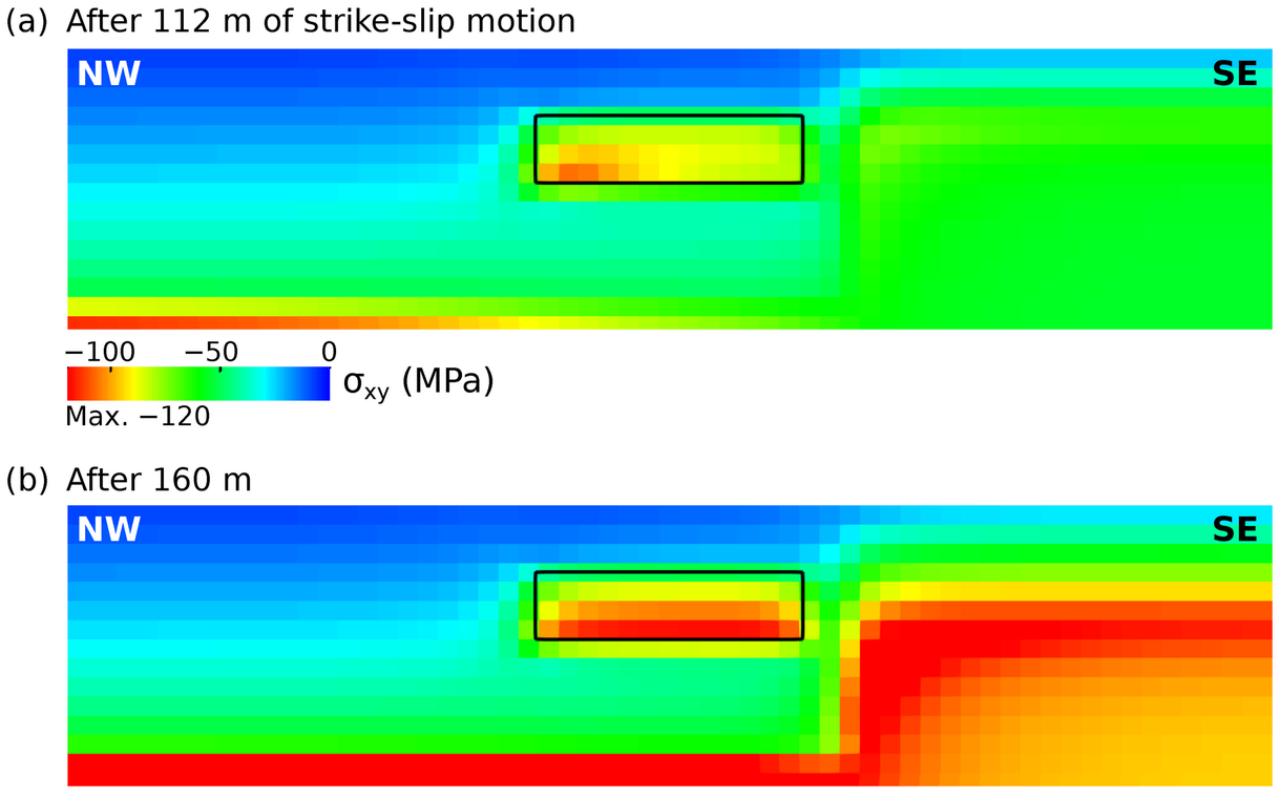
Perrin et al.; Figure 4

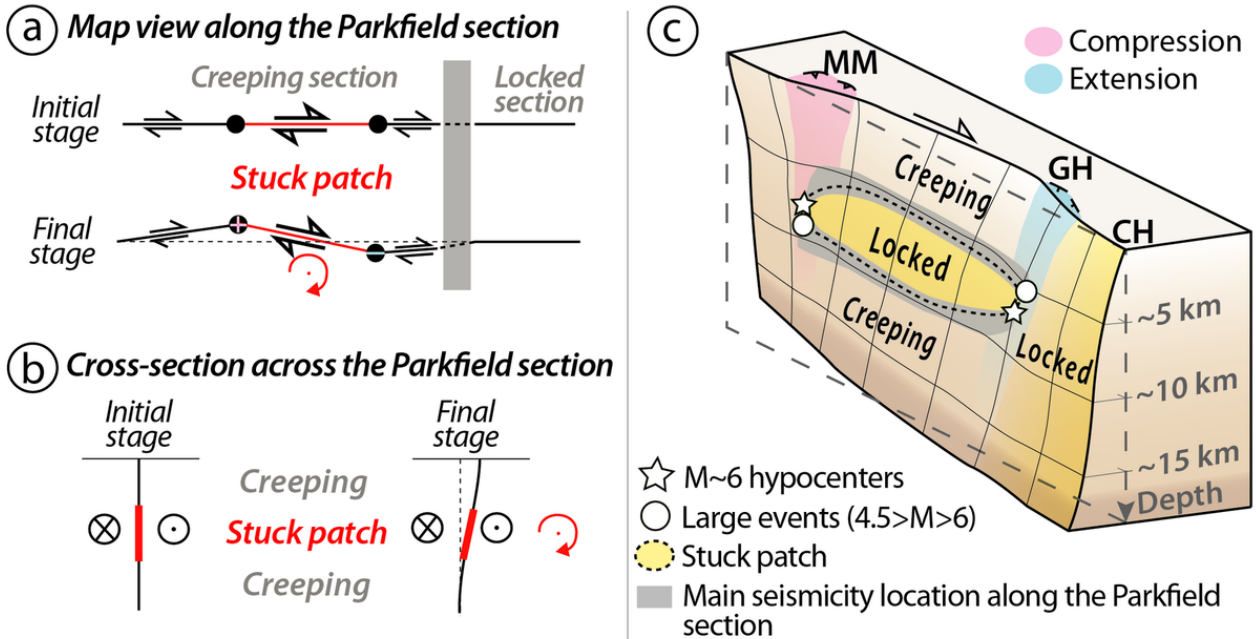


Perrin et al.; Figure 5

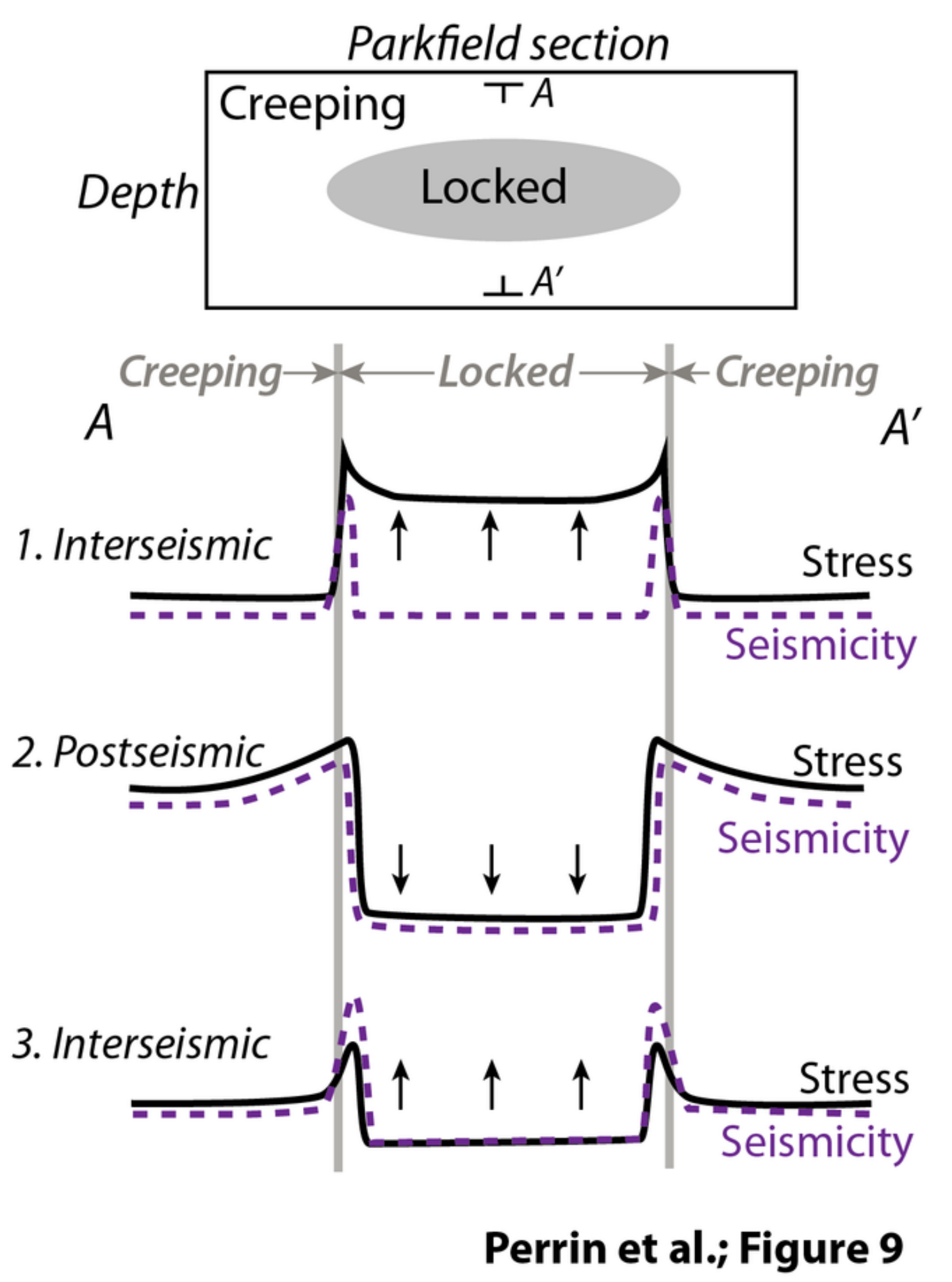


Perrin et al.; Figure 6


(a) After 112 m of strike-slip motion
NW
SE
−100
−50
0
σxy (MPa)
Max. −120
(b) After 160 m
NW
SE



Perrin et al.; Figure 8



Perrin et al.; Figure 9